Science Advances
AAAS

advances.sciencemag.org/cgi/content/full/6/29/eaba8656/DC1

Supplementary Materials for

Reconfigurable Floquet elastodynamic topological insulator based on synthetic angular momentum bias

Amir Darabi, Xiang Ni, Michael Leamy*, Andrea Alù*

*Corresponding author. Email: aalu@gc.cuny.edu (A.A.); michael.leamy@me.gatech.edu (M.L.)

Published 17 July 2020, *Sci. Adv.* **6**, eaba8656 (2020)
DOI: 10.1126/sciadv.aba8656

This PDF file includes:

SUPPLEMENTARY NOTE 1: DISPERSION CURVES

System with no modulation:

A composite structure is made by bonding 0.5 mm thick piezoelectric disks (PZT) to a host layer (PLA) with the thickness of 0.5 mm. Both the disks and the host layer are modeled as linear isotropic materials rigidly bonded to each other. To plot the band structure of the unit cell, one should solve the equations of motion for this composite structure governed by,

$$\rho\ddot{\mathbf{U}} = \nabla.S \tag{S-1}$$

$$S = \mathbf{c}(E) : \varepsilon(\mathbf{U}), \tag{S-2}$$

where $\mathbf{U}(x, y, z) = u\hat{i} + v\hat{j} + w\hat{k}$ is the displacement vector, ρ the density, $\nabla.$ the divergence operator, S the stress matrix, $\mathbf{c}(E)$ is the fourth order elasticity tensor for either isotropic material, E the modulus of elasticity, and $\varepsilon(\mathbf{U})$ the strain matrix. Figure S-2(a) depicts a 0.5 mm thick PLA ($E = 3.5\ GPa$, $\rho = 1300\ kg/m^3$, $\nu = 0.3$) hexagonal unit cell bonded to six piezoelectric disks ($E_p^E = 72\ GPa$, $\rho = 7800\ kg/m^3$, $C_p = 1.5\ nF$, $k_{31} = 0.31$), each with thickness 0.5 mm and diameter 7 mm, Fig. S-2(b) depicts the first Brillouin zone, and Fig. S-2(c) provides the system's band structure in the absence of modulation computed using COMSOL Multiphysics. The unit cells are repeated along the lattice vectors $\mathbf{a_1} = L\hat{i}$ and $\mathbf{a_2} = L/2\hat{i} + \sqrt{3}L/2\hat{j}$ to form the entire periodic structure. Floquet boundary conditions in COMSOL Multiphysics, with appropriate destinations on the edges, are used to model the periodicity of the unit cell in the aforementioned directions. The dispersion curves are then computed by sweeping the wavevector along the boundaries of the first irreducible Brillouin zone (blue triangular area in Fig. S-2(b)),

$$\Gamma = (0, 0) \tag{S-3}$$

$$M = (0, 2\pi/\sqrt{3}) \tag{S-4}$$

$$K = (2\pi/3, 2\pi/\sqrt{3}). \tag{S-5}$$

As shown in Fig. S-2(c), multiple Dirac cones are observed at the K-point. As depicted, due to the complexity of the system proposed herein, more modes are present compared to the theoretical model designed in [23], where the authors simply studied a lattice of six acoustic resonators with six degrees of freedom. Since all of these modes will be folded after applying time modulation, difficulties arise in finding a topological bandgap to protect edges states. Note that the bands falling within the frequency range of interest are plotted in blue.

Negative capacitance:

One possible way to vary material properties in time is to employ shunted piezoelectric disks. Figure S-1 depicts a schematic of a piezoelectric disk attached to an external circuit. Accordingly, when a piezoelectric patch is connected to an active circuit with the capacitance of $-C'$ (see Fig. S-1), the elastic modulus is obtained as [38-39],

$$E_m = E_E^P \frac{C' - C_p^T}{C' - C_p^S}, \tag{S-6}$$

where E_E^P denotes the Young's modulus of the PZT disk when the electrodes are short circuited, C_p^T the stress-free capacitance, $C_p^S = C_p^T(1 - k_{31}^2)$ the strain-free capacitance, and k_{31} the piezoelectric coupling coefficient for the longitudinal straining of a through-the-thickness polarized patch, respectively. In the absence of modulation, PZT patches are open-circuited; hence, the elastic modulus is obtained by placing $C' = 0$ in Eq. S-6,

$$E_0 = E_p^E \frac{1}{1 - k_{31}^2}. \tag{S-7}$$

The equivalent negative capacitance is specified by,

$$-C' = -\frac{R_2 C_0}{R_1}, \tag{S-8}$$

where R_1 and R_2 are the resistors connected to the op-amp, and C_0 is the paralleled capacitor. The coupled PZT and circuit are only stable when $C' > C_p^T$ [41]. In addition, to prevent saturation of the capacitor (which can also lead to

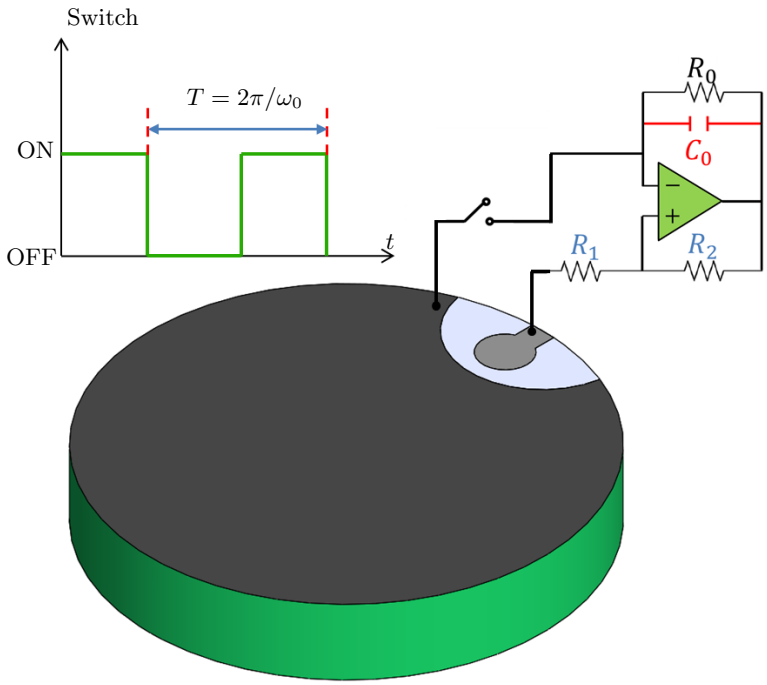

FIG. S-1. **Schematic of a shunted piezoelectric disk and its connected circuit**. The switch placed between the PZT disk and the negative capacitance circuit varies the effective Young's modulus between E_0 and E_m at the frequency of $f_0 = 1/T$.

instability), a resistor (R_0) with a relatively large resistance compared to R_1 and R_2 is paralleled with the capacitor [42]. Finally, as shown in Fig. S-1, by placing a switch between the piezoelectric and the circuit, we can modulate the PZT's effective elastic modulus between E_0 and E_m by ON/OFF operation of the switch at the fundamental frequency $f_0 = 1/T$.

System with modulation:

The discussion below holds for the piezoelectric subdomain undergoing time modulation; the PLA subdomain continues to be governed by Eq. S-1. In order to model the system with time modulation, we alter the modeled stiffness of the piezoelectric disks from the open-circuit value, E_0, to the closed-circuit value (for optimal bandgap opening), E_m, using a period $T = 2\pi/\omega_0$,

$$E(\mathbf{r}, t) = E_0 + \frac{\delta E}{2}(\mathbf{sgn}[cos(\omega_0 t + \phi(\mathbf{r})] - 1), \tag{S-9}$$

where **sgn** denotes the sign function taking either -1 or 1 and $\delta E = E_0 - E_m$ denotes the modulation depth. This function can be expressed using its Fourier decomposition,

$$E(r, t) = (E_0 - \frac{\delta E}{2}) - \frac{\delta E}{2} \sum_{n=-(2k+1)}^{2k+1} \bar{a}_n \tag{S-10}$$

$$\bar{a}_n = \mathbf{sgn}(n) \frac{4ie^{i(n\omega_0 t + n\phi(\mathbf{r}))}}{n\pi}, \tag{S-11}$$

where $i = \sqrt{-1}$ is the unit imaginary number, and n takes only odd values. Since the system is modulated with the frequency of $f_0 = \omega_0/2\pi$, the solution of Eq. S-1 will be in the form of,

$$U(\mathbf{r}, t) = \sum_l U_l(\mathbf{r}) e^{i(\omega + l\omega_0)t}. \tag{S-12}$$

Replacing Eq. S-12 in the main equation of motion (i.e., Eq. S-1), and using the Floquet-Bloch theorem in time, we obtain the following infinite set of coupled time-independent differential equations for the harmonics $U_l(r)$:

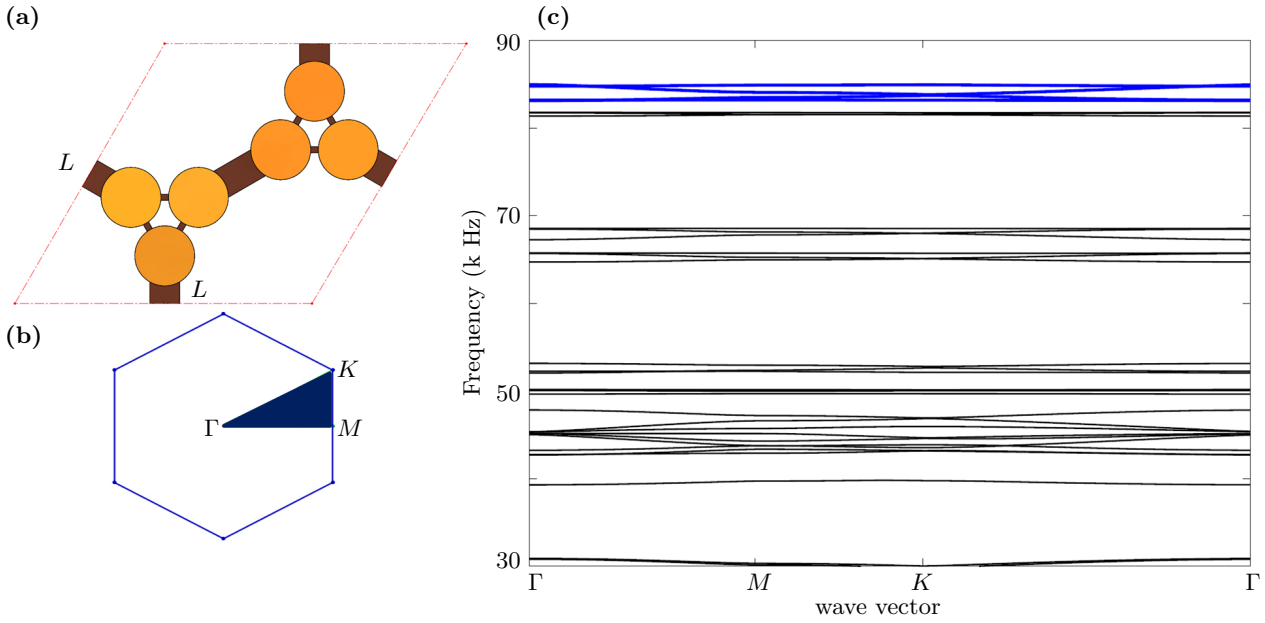

FIG. S-2. **Detailed band structure of the system without modulation. (a)** Schematic of the proposed hexagonal unit cell (with characteristic size L), composed of a PLA host layer with six bonded piezoelectric disks, **(b)** first Brillouin zone of the proposed hexagonal unit cell, **(c)** band structure of the hexagonal unit cell in the absence of modulation. Blue curves exhibit the frequency range of interest for which modulation will be applied.

$$-(\omega - n\omega_0)^2 \rho \mathbf{U}_l(\mathbf{r}) = \nabla.\left[\mathbf{c}\Big(E_0 - \frac{\delta E}{2}\Big) : \varepsilon\Big(\mathbf{U}_l(\mathbf{r})\Big)\right] + \sum_{n=-(2k+1)}^{2k+1} \nabla.\left[\mathbf{c}\Big(\frac{\delta E}{2}\Big) : \varepsilon\Big(\mathbf{U}_{n-l}(\mathbf{r})\Big)\right] \bar{a}_n e^{in\phi(\mathbf{r})}. \quad \text{(S-13)}$$

In order to solve these independent equations, the system in Eq. S-13 is truncated to the fifth harmonic $l = \{-2, -1, 0, 1, 2\}$, and fifth term of Eq. S-10 as $n = \{-3, -1, 0, 1, 3\}$, which captures adequately the response in the frequency range of interest. This equation is then inputted into COMSOL Multiphysics (Solid Mechanics Module), after transformation to the weak form, where these fully coupled equations are directly computed in the (quasi-)frequency domain. Figure S-3 plots the band structure of the system computed from Eq. S-13 when modulation is applied at a frequency of $f_0 = 50\ kHz$ and modulation depth of $\delta E = 0$. It is important to choose the modulation frequency such that the folded bands do not interfere with the original ones at the location of the desired Dirac cone. As observed, in addition to the original dispersion curves (plotted in blue), folded bands are present where red curves correspond to $l = 1$, and green correspond to $l = -1$, respectively. Although Eq. S-13 is computed using five harmonics, only three of them fall within the plotted frequency range (i.e., 30-90 kHz). This clearly documents that for the targeted Dirac cone (at approximately 84 kHz), no folded modes interfere with the frequency range of interest (marked with a black box).

SUPPLEMENTARY NOTE 2: CHERN NUMBER

For any dispersion curve bounding the topological bandgap, the Berry connection is defined as [43],

$$\boldsymbol{\mathscr{A}}(\mathbf{k}) \equiv \langle \mathbf{U}(\mathbf{k}) | i \nabla_{\mathbf{k}} | \mathbf{U}(\mathbf{k}) \rangle, \quad \text{(S-14)}$$

where $\mathbf{U}(\mathbf{k})$ denotes the mass-normalized displacement of the eigenmode with harmonic index $l = 0$ computed at the wavevector $\mathbf{k}$, $\nabla_{\mathbf{k}} \equiv \frac{\partial}{\partial_{kx}}\hat{i} + \frac{\partial}{\partial_{ky}}\hat{j}$, and $i \equiv \sqrt{-1}$ is the unit imaginary number. The Berry curvature of a given mode is defined as $\boldsymbol{\mathscr{F}} \equiv \nabla_{\mathbf{k}} \times \boldsymbol{\mathscr{A}}$. Figure S-4 displays the Berry curvature of the system shown in Fig. 1(e) at the optimal value of the bandgap. Finally, the total Chern number of each mode is computed as the integral of the Berry curvature over the entire Brillouin zone,

$$C \equiv \frac{1}{2\pi} \iint \left(\frac{\partial \mathscr{A}_{k_y}}{\partial k_x} - \frac{\partial \mathscr{A}_{k_x}}{\partial k_y} \right) dk_x\, dk_y \quad \text{(S-15)}$$

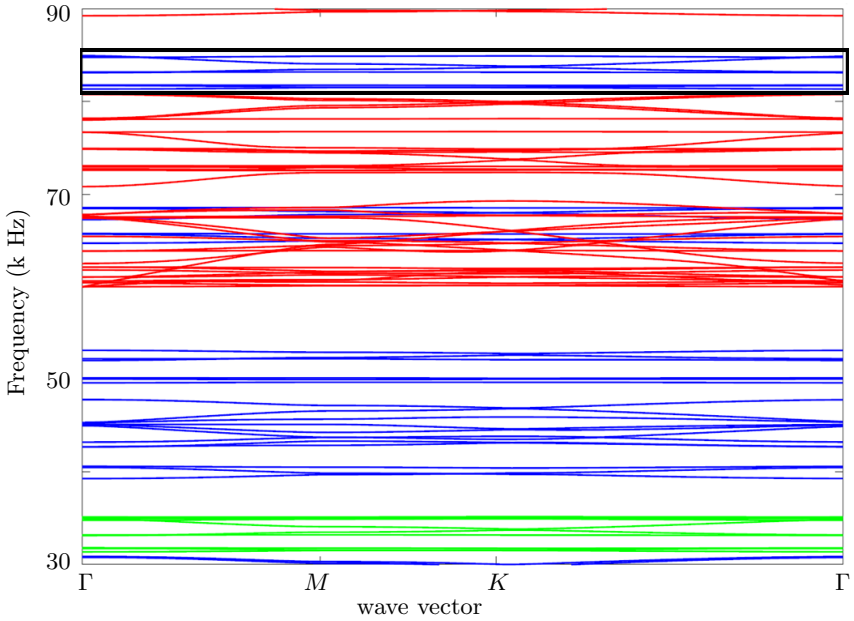

FIG. S-3. **Band structure of the hexagonal unit cell in the presence of modulation with zero depth.** Blue curves exhibit the original modes while red ($l = 1$) and green ($l = -1$) lines exhibit folded modes.

The required integration can be computed numerically using two *trapz* functions in Matlab. For the system proposed in this study, the total Chern numbers are computed to be $\{+1, 0, 0, -1\}$.

SUPPLEMENTARY NOTE 3: TOPOLOGY OF FLOQUET SYSTEMS

The aim of this section is to prove the accuracy of the presented approach in the previous section, to compute the Chern number by only considering the zeroth order of modulation. This is done by developing an analytical approach, where we establish a connection between the Chern number obtained from the harmonic series of Floquet states (in the above section), and the stroboscopic effective Hamiltonian. First, we start with the general form of the eigenvalue problem as,

$$i\partial_t \psi(\mathbf{k}, t) = \mathscr{H}(\mathbf{k}, t)\psi(\mathbf{k}, t), \tag{S-16}$$

where $\psi(\mathbf{k}, t)$ describes the eigenstate at arbitrary time t, and $\mathscr{H}(\mathbf{k}, t)$ is the Hamiltonian of the system in momentum space. The evolution then is obtained from S-16 as, $\mathscr{U}(t) = \mathscr{T} \exp(-i \int_0^t \mathscr{H}(\mathbf{k}, t')dt'$, which defines the time-dependent state from initial state to be

$$\psi(\mathbf{k}, t) = \mathscr{U}(t - t_0)\psi(\mathbf{k}, t_0). \tag{S-17}$$

When a periodic temporal modulation is applied to the system with the period of T ($\mathscr{H}(\mathbf{k}, t) = \mathscr{H}(\mathbf{k}, \mathrm{T} + t)$), the stroboscopic Hamiltonian can be extracted from evolution operator to be time independent,

$$\mathscr{U}(\mathrm{T})\psi(\mathbf{k}, t_0) = \exp(-i\mathscr{H}_{\mathrm{eff}}\mathrm{T})\psi(\mathbf{k}, t_0). \tag{S-18}$$

Namely, the expression of such static Hamiltonian is $\mathscr{H}_{\mathrm{eff}} = \frac{i}{\mathrm{T}} \log \mathscr{U}(\mathrm{T})$, which effectively describes the average effect of the dynamics and contains the information of topology of the Floquet system. Then topological invariant is revealed by calculating the Chern number defined in Eq. (S-15) from the static eigenstates. The following effort is to show such topology can be equivalently represented by the Harmonic series of time-dependent Floquet states. Next we apply Bloch-Floquet theorem to the wavefunction in eq. (S-16) as below,

$$\psi(\mathbf{k}, t) = e^{-i\omega t}\phi(\mathbf{k}, t), \tag{S-19}$$

where Floquet state $\phi(\mathbf{k}, t)$ is periodic in time such that $\phi(\mathbf{k}, t) = \phi(\mathbf{k}, \mathrm{T} + t)$, and ω is the quasi-frequency of the Floquet states with the period of $\omega_0 = \frac{2\pi}{\mathrm{T}}$. Replacing Eq. S-19 into Eq. S-16 will introduce the new form of eigenvalue problem under the Floquet state as,

$$\mathscr{H}_{\mathrm{F}}\phi(\mathbf{k}, t) = \omega\phi(\mathbf{k}, t), \tag{S-20}$$

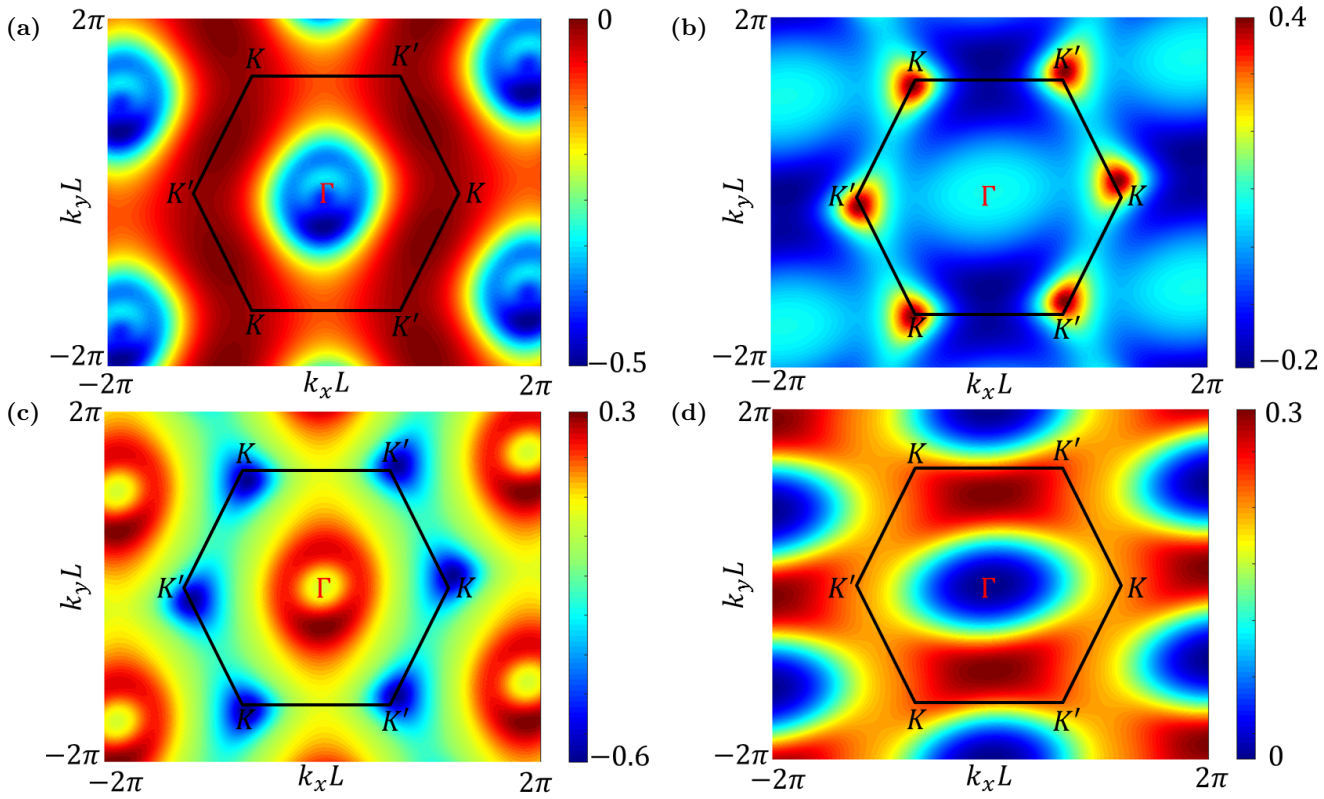

FIG. S-4. **Topological properties of the proposed system.** The Berry curvature of the system proposed in Fig. 1(e) for the four bands bounding the topological bandgaps in the frequency range of interest.

where $\mathscr{H}_{\mathrm{F}} = \mathscr{H}(\mathbf{k}, t) - i\partial_t$ is the Floquet Hamiltonian. Considering the periodic behavior of the system, Eq. (S-18) will appear in the new form as,

$$\psi(\mathbf{k}, \mathrm{T} + t_0) = \exp(-i\mathscr{H}_{\mathrm{eff}}\mathrm{T})\psi(\mathbf{k}, t_0). \tag{S-21}$$

Finally, replacing back Eq. (S-19) into (S-21) results in,

$$e^{-i\omega(\mathrm{T}+t_0)}\phi(\mathbf{k}, \mathrm{T} + t_0) = \exp(-i\mathscr{H}_{\mathrm{eff}}\mathrm{T})e^{-i\omega t_0}\psi(\mathbf{k}, t_0). \tag{S-22}$$

which can be then simplified by applying Taylor expansion to both sides as,

$$\mathscr{H}_{\mathrm{eff}}\phi(\mathbf{k}, t) = \omega\phi(\mathbf{k}, t), \tag{S-23}$$

This final form reveals the both Floquet Hamiltonian and stroboscopic effective Hamiltonian share the same set of eigenstates. Since Floquet states are periodic in time, we apply Fourier transform to these states in (S-23), therefore,

$$\mathscr{H}_{\mathrm{eff}} \sum_l \phi(\mathbf{k}, l)e^{il\omega_0 t} = \omega \sum_l \phi(\mathbf{k}, l)e^{il\omega_0 t}, \tag{S-24}$$

where l is an integer. In order for (S-24) to be valid, each harmonic function $\phi(\mathbf{k}, l)$ needs to satisfy $\mathscr{H}_{\mathrm{eff}}\phi(\mathbf{k}, l) = \omega\phi(\mathbf{k}, l)$, such that it is reasonable to use arbitrary $\phi(\mathbf{k}, l)$ to characterize the topology of the Floquet system. Especially, when $l = 0$, it corresponds to the analog first Brillouin zone of quasi-frequency. When the dynamics of the Floquet system are approximately described by the coupled equations of finite series harmonics, the Chern number obtained from eigenstates $\phi(\mathbf{k}, 0)$ will most accurately describe the topology of the Floquet system. This clearly confirms the accuracy of the approach in the previous section to compute the Chern number by only considering the zeroth order of modulation (i.e., ω_0).

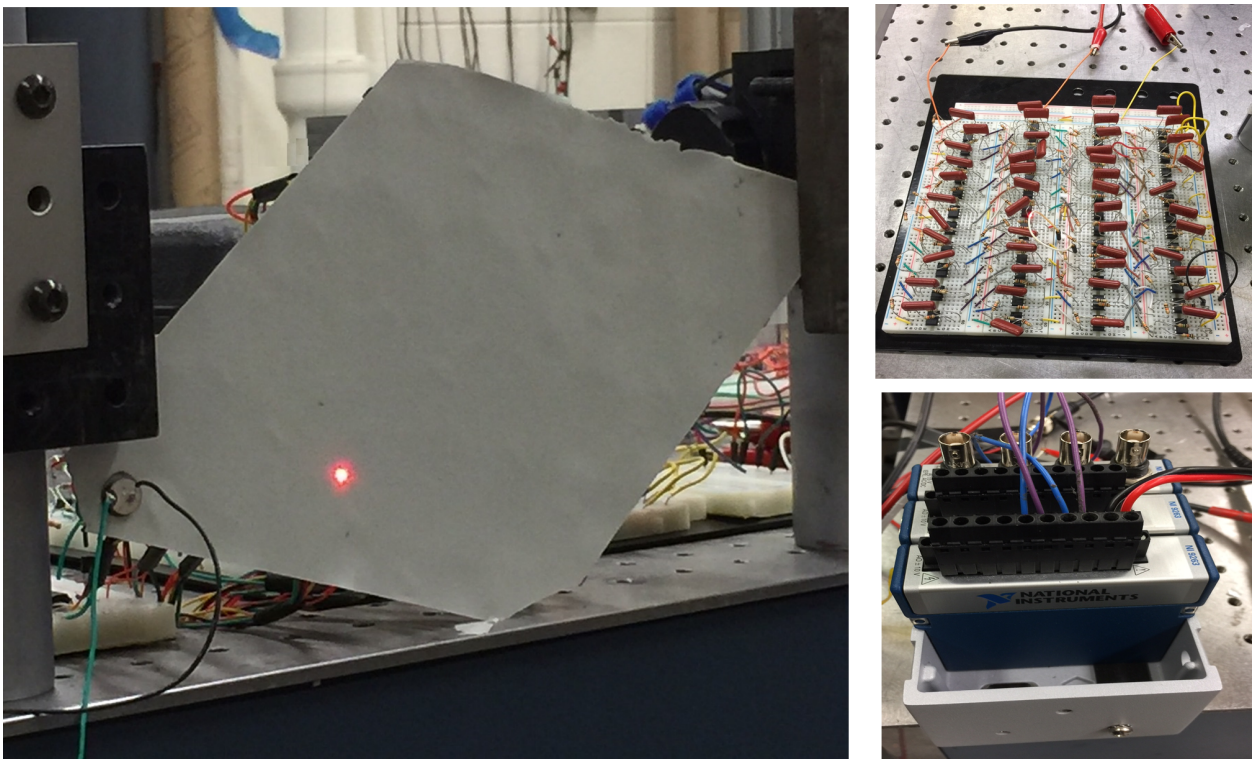

FIG. S-5. **Fabricated experimental setup.** On the left: the tested structure (back side) after being wired to the circuit. Reflective tape is used in measuring the displacement via a scanning laser Doppler vibrometer (red spot). An exciting PZT disk (lower left in subfigure) stimulates the system at frequency f_0. On the right: the circuits used to provide negative capacitance to the PZT disks. Photo Credit: Amir Darabi, Georgia Institute of Technology.

SUPPLEMENTARY NOTE 4: EXPERIMENT

Setup:

Figure S-5 depicts the back-side of the fabricated structure (on the left) and the connected circuit (on the right) that are used to measure the wave-response of the field. See Fig. 3a in the manuscript for the front side. The composite structure is realized from a 0.5 mm thick PLA layer with one-hundred and fifty glued (by 3M DP270 Epoxy Adhesive) piezoelectric disks.

Time snapshots of experimental results:

Figures S-6 and S-7 plot time snap-shots of the experimentally-measured wavefield for the horizontal and triangular interfaces reported in the manuscript.

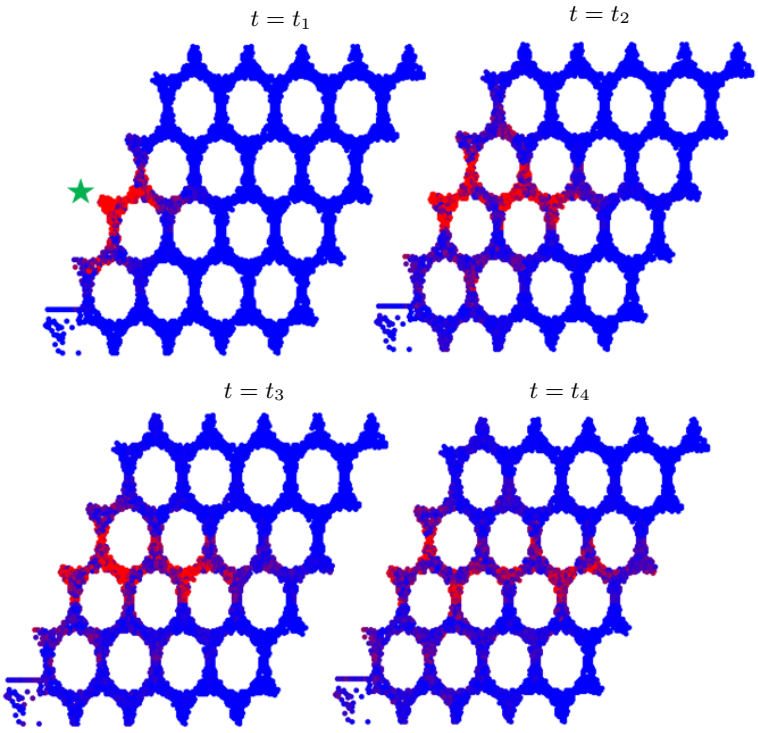

FIG. S-6. **Time snapshots of experimental results.** Experimentally-measured displacement wavefield with a horizontal interface (depicted in Fig. 4(a) of the manuscript) captured at different times due to excitation by a source with frequency 87 kHz kHz. The location of source is marked withe the green star.

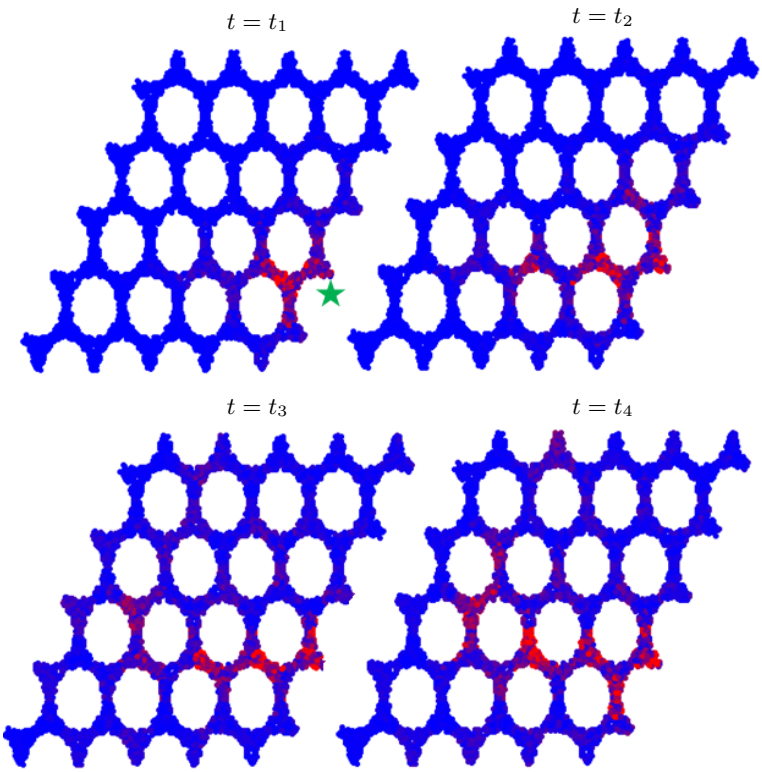

FIG. S-7. **Time snapshots of experimental results.** Experimentally-measured displacement wavefield with a triangular interface (depicted in Fig. 4(b) of the manuscript) captured at different times due to excitation by a source with frequency 87 kHz kHz. The location of source is marked withe the green star.

REFERENCES AND NOTES

1. C. L. Kane, E. J. Mele, Quantum spin Hall effect in graphene. *Phys. Rev. Lett.* **95**, 226801 (2005).

2. M. Z. Hasan C. L. Kane, Colloquium: Topological insulators. *Rev. Mod. Phys.* **82**, 3045 (2010).

3. X.-L. Qi, S.-C. Zhang, Topological insulators and superconductors. *Rev. Mod. Phys.* **83**, 1057 (2011).

4. F. D. M. Haldane, S. Raghu, Possible realization of directional optical waveguides in photonic crystals with broken time-reversal symmetry. *Phys. Rev. Lett.* **100**, 013904 (2008).

5. Z. Wang, Y. D. Chong, J. D. Joannopoulos, M. Soljačić, Reflection-free one-way edge modes in a gyromagnetic photonic crystal. *Phys. Rev. Lett.* **100**, 013905 (2008).

6. A. B. Khanikaev, S. H. Mousavi, W.-K. Tse, M. Kargarian, A. H. MacDonald, G. Shvets, Photonic topological insulators. *Nat. Mater.* **12**, 233 (2013).

7. L. Lu, J. D. Joannopoulos, M. Soljačić, Topological photonics. *Nat. Photonics* **8**, 821 (2014).

8. M. Hafezi, S. Mittal, J. Fan, A. Migdall, J. M. Taylor, Imaging topological edge states in silicon photonics. *Nat. Photonics* **7**, 1001 (2013).

9. A. B. Khanikaev, G. Shvets, Two-dimensional topological photonics. *Nat. Photonics* **11**, 763 (2017).

10. T. Ozawa, H. M. Price, A. Amo, N. Goldman, M. Hafezi, L. Lu, M. C. Rechtsman, D. Schuster, J. Simon, O. Zilberberg, I. Carusotto, Topological photonics. *Rev. Mod. Phys.* **91**, 015006 (2019).

11. J. Paulose, B. G.-g. Chen, V. Vitelli, Topological modes bound to dislocations in mechanical metamaterials. *Nat. Phys.* **11**, 153–156 (2015).

12. B. G.-g. Chen, N. Upadhyaya, V. Vitelli, Nonlinear conduction via solitons in a topological mechanical insulator. *Proc. Natl. Acad. Sci. U.S.A.* **111**, 13004–13009 (2014).

13. S. H. Mousavi, A. B. Khanikaev, Z. Wang, Topologically protected elastic waves in phononic metamaterials. *Nat. Commun.* **6**, 8682 (2015).

14. R. Süsstrunk, S. D. Huber, Observation of phononic helical edge states in a mechanical topological insulator. *Science* **349**, 47 (2015).

15. R. Fleury, D. L. Sounas, C. F. Sieck, M. R. Haberman, A. Alù, Sound isolation and giant linear nonreciprocity in a compact acoustic circulator. *Science* **343**, 516 (2014).

16. Z. Yang, F. Gao, X. Shi, X. Lin, Z. Gao, Y. Chong, B. Zhang, Topological acoustics. *Phys. Rev. Lett.* **114**, 114301 (2015).

17. M. Miniaci, R. K. Pal, B. Morvan, M. Ruzzene, Experimental observation of topologically protected helical edge modes in patterned elastic plates. *Phys. Rev. X* **8**, 031074 (2018).

18. C. L. Kane, T. C. Lubensky, Topological boundary modes in isostatic lattices. *Nat. Phys.* **10**, 39 (2014).

19. D. Z. Rocklin, B. G.-g. Chen, M. Falk, V. Vitelli, T. C. Lubensky, Mechanical Weyl modes in topological Maxwell lattices. *Phys. Rev. Lett.* **116**, 135503 (2016).

20. O. Stenull, C. L. Kane, T. C. Lubensky, Topological phonons and Weyl lines in three dimensions. *Phys. Rev. Lett.* **117**, 068001 (2016).

21. T. Kariyado, Y. Hatsugai, Manipulation of dirac cones in mechanical graphene. *Sci. Rep.* **5**, 18107 (2015).

22. A. B. Khanikaev, R. Fleury, S. H. Mousavi, A. Alù, Topologically robust sound propagation in an angular-momentum-biased graphene-like resonator lattice. *Nat. Commun.* **6**, 8260 (2015).

23. R. Fleury, A. B. Khanikaev, A. Alu, Floquet topological insulators for sound. *Nat. Commun.* **7**, 11744 (2016).

24. E. Prodan, C. Prodan, Topological phonon modes and their role in dynamic instability of microtubules. *Phys. Rev. Lett.* **103**, 248101 (2009).

25. P. Wang, L. Lu, K. Bertoldi, Topological phononic crystals with one-way elastic edge waves. *Phys. Rev. Lett.* **115**, 104302 (2015).

26. L. M. Nash, D. Kleckner, A. Read, V. Vitelli, A. M. Turner, W. T. M. Irvine, Topological mechanics of gyroscopic metamaterials. *Proc. Natl. Acad. Sci. U.S.A.* **112**, 14495 (2015).

27. Y.-T. Wang, P.-G. Luan, S. Zhang, Coriolis force induced topological order for classical mechanical vibrations. *New J. Phys.* **17**, 073031 (2015).

28. X. Ni, C. He, X.-C. Sun, X.-p. Liu, M.-H. Lu, L. Feng, Y.-F. Chen, Topologically protected one-way edge mode in networks of acoustic resonators with circulating air flow. *New J. Phys.* **17**, 053016 (2015).

29. R. Chaunsali, E. Kim, A. Thakkar, P. G. Kevrekidis, J. Yang, Demonstrating an *in situ* topological band transition in cylindrical granular chains. *Phys. Rev. Lett.* **119**, 024301 (2017).

30. N. Swinteck, S. Matsuo, K. Runge, J. O. Vasseur, P. Lucas, P. A. Deymier, Bulk elastic waves with unidirectional backscattering-immune topological states in a time-dependent superlattice. *J. Appl. Phys.* **118**, 063103 (2015).

31. M. C. Rechtsman, J. M. Zeuner, Y. Plotnik, Y. Lumer, D. Podolsky, F. Dreisow, S. Nolte, M. Segev, A. Szameit, Photonic Floquet topological insulators. *Nature* **496**, 196 (2013).

32. J.-i. Inoue, A. Tanaka, Photoinduced transition between conventional and topological insulators in two-dimensional electronic systems. *Phys. Rev. Lett.* **105**, 017401 (2010).

33. N. H. Lindner, G. Refael, V. Galitski, Floquet topological insulator in semiconductor quantum wells. *Nat. Phys.* **7**, 490 (2011).

34. Y.-G. Peng, C.-Z. Qin, D.-G. Zhao, Y.-X. Shen, X.-Y. Xu, M. Bao, H. Jia, X.-F. Zhu, Experimental demonstration of anomalous Floquet topological insulator for sound. *Nat. Commun.* **7**, 13368 (2016).

35. N. A. Estep, D. L. Sounas, J. Soric, A. Alù, Magnetic-free non-reciprocity and isolation based on parametrically modulated coupled-resonator loops. *Nat. Phys.* **10**, 923 (2014).

36. H. Lamb, On waves in an elastic plate. *Proc. R. Soc. Lond. A* **93**, 114 (1917).

37. S. Behrens, A. J. Fleming, S. O. R. Moheimani, A broadband controller for shunt piezoelectric damping of structural vibration. *Smart Mater. Struct.* **12**, 18 (2003).

38. B. S. Beck, K. A. Cunefare, M. Collet, The power output and efficiency of a negative capacitance shunt for vibration control of a flexural system. *Smart Mater. Struct.* **22**, 065009 (2013).

39. N. W. Hagood, A. von Flotow, Damping of structural vibrations with piezoelectric materials and passive electrical networks. *J. Sound Vib.* **146**, 243 (1991).

40. Y. Hatsugai, Chern number and edge states in the integer quantum Hall effect. *Phys. Rev. Lett.* **71**, 3697 (1993).

41. B. De Marneffe, A. Preumont, Vibration damping with negative capacitance shunts: Theory and experiment. *Smart Mater. Struct.* **17**, 035015 (2008).

42. G. Trainiti, Y. Xia, J. Marconi, G. Cazzulani, A. Erturk, M. Ruzzene, Time-periodic stiffness modulation in elastic metamaterials for selective wave filtering: Theory and experiment. *Phys. Rev. Lett.* **122**, 124301 (2019).

43. H. C. P. Adrian, "Electronic band structure in topological textures," thesis, The Chinese University of Hong Kong (2011).